Geophysical Journal International

Geophys. J. Int. (2024) **238,** 960–973
Advance Access publication 2024 June 05
GJI Applied and Marine Geophysics

https://doi.org/10.1093/gji/ggae197

Joint inversion of induced polarization and hydraulic tomography data for hydraulic conductivity imaging

Lukas Römhild [1], Gianluca Fiandaca [2] and Peter Bayer [1]

[1] *Applied Geology, Institute of Geosciences and Geography, Martin Luther University Halle-Wittenberg, Von-Seckendorff-Platz 3, 06120 Halle (Saale), Germany. E-mail: lukas.roemhild@geo.uni-halle.de*
[2] *The EEM Team for Hydro & eXploration, Department of Earth Sciences "Ardito Desio", Università degli Studi di Milano, Via Sandro Botticelli 23, 20133 Milano, Italy*

Accepted 2024 May 30. Received 2024 April 30; in original form 2024 January 23

SUMMARY

For accurate modelling of groundwater flow and transport processes within an aquifer, precise knowledge about hydraulic conductivity K and its small-scale heterogeneities is fundamental. Methods based on pumping tests, such as hydraulic tomography (HT), allow for retrieving reliable K-estimates, but are limited in their ability to image structural features with high resolution, since the data from time-consuming hydraulic tests are commonly sparse. In contrast, geophysical methods like induced polarization (IP) can potentially yield structural images of much higher resolution, but depend on empirical petrophysical laws that may introduce significant uncertainties to the K-estimation. Therefore, this paper presents a joint inversion procedure for both HT and IP data, which allows for combining the complementary abilities of both methods. Within this approach, a traveltime inversion is applied to the HT data, while the IP inversion is based on a full-decay time-domain forward response, as well as a reparametrization of the Cole–Cole model to invert for K directly. The joint inversion is tested on a synthetic model mimicking horizontally layered sediments, and the results are compared with the individual HT and IP inversions. It is shown that jointly inverting both data sets consistently improves the results by combining the complementary sensitivities of the two methods, and that the inversion is more robust against changes in the experimental setups. Furthermore, we illustrate how a joint inversion approach can correct biases within the petrophysical laws by including reliable K-information from hydraulic tests and still preserving the high-resolution structural information from IP. The different inversion results are compared based on the structural similarity index (SSIM), which underlines the robustness of the joint inversion compared to using the data individually. Hence, the combined application of HT and IP within field surveys and a subsequent joint inversion of both data sets may improve our understanding of hydraulically relevant subsurface structures, and thus the reliability of groundwater modelling results.

Key words: Electrical properties; Permeability and porosity; Induced polarization; Joint inversion; Hydrogeophysics; Tomography.

1 INTRODUCTION

The hydraulic properties of the near-surface Earth have long been a target of geophysical research (e.g. Binley *et al.* 2015). In particular, precise knowledge about the spatial distribution of the hydraulic conductivity K in shallow aquifers is crucial for predicting flow and transport processes correctly (e.g. Comunian *et al.* 2011; Refsgaard *et al.* 2012; You *et al.* 2020). Classically, in the hydrogeological community, this information is inferred from different types of hydraulic tests. Among them, hydraulic tomography (HT) has been established as a method that is able to image the spatial distribution of K between two or more boreholes using a tomographic configuration (Yeh & Liu 2000). The method is based on sequential pumping experiments in several depth intervals within one borehole, while the transient pressure or hydraulic head response is recorded in other nearby intervals at different depths. A broad range of inversion approaches is available to infer the hydraulic parameters from the HT data, which are based either on discrete fracture network models (e.g. Klepikova *et al.* 2014; Somogyvári *et al.* 2019; Klepikova *et al.* 2020; Fischer *et al.* 2020; Ringel *et al.* 2022; Römhild *et al.* 2024), or on heterogeneous continuum models (e.g. Illman *et al.* 2009; Berg & Illman 2011; Cardiff *et al.* 2013; Zha *et al.* 2015;

Fischer *et al.* 2017; Somogyvari & Bayer 2017; Cardiff *et al.* 2019; Zhao *et al.* 2019; Ren *et al.* 2021; Luo *et al.* 2023; Zhao *et al.* 2023), while the latter is most suitable for porous media. In particular, continuum-based traveltime inversion (Brauchler *et al.* 2003; Hu *et al.* 2011; Brauchler *et al.* 2013; Yang *et al.* 2020; Liu *et al.* 2022) is considered appealing due to its computational efficiency.

The main advantage of these methods is the direct link between the measured hydraulic data and the desired hydraulic parameters, which does not require using petrophysical approximations. Therefore, the overall quantification of K is highly reliable, reflecting the true hydraulic characteristics of the aquifer (e.g. Zhao *et al.* 2015). However, conducting these pumping tests in the field can be time-consuming and expensive, with a single test typically taking several hours (e.g. Berg & Illman 2013), so that only a small number of them is practically feasible. Therefore, the ability to image the hydraulic parameters with high resolution is mostly limited due to a low data density and thus a high degree of non-uniqueness of the inverse problem (Bohling & Butler 2010). Furthermore, HT experiments are most sensitive to high-K zones as the major flow paths within the aquifer, but low-K heterogeneities are more difficult to image.

In contrast, hydrogeophysical measurements can often be conducted more time- and cost-efficiently, making it more feasible to image subsurface heterogeneities with higher resolution. Particularly, induced polarization (IP) has the potential to reliably map the distribution of K in near-surface aquifers (Slater 2007; Binley & Slater 2020). Based on the conceptual similarities between groundwater flow and electrical conduction in porous media, petrophysical relations linking hydraulic and electrical parameters have been derived from laboratory experiments (e.g. Börner *et al.* 1996; Slater & Lesmes 2002; Binley *et al.* 2005; Revil & Florsch 2010; Titov *et al.* 2010; Revil *et al.* 2012; Attwa & Günther 2013; Weller *et al.* 2015; Robinson *et al.* 2018). The resulting equations can either be applied to the electrical parameters retrieved from the IP inversion in a separate step (Hördt *et al.* 2009; Attwa & Günther 2013; Maurya *et al.* 2018a), or directly be incorporated into the inversion procedure (Fiandaca *et al.* 2018b; Römhild *et al.* 2022a). For the latter, a re-parametrization of the Cole–Cole model (Cole & Cole 1941; Pelton *et al.* 1978; Tarasov & Titov 2013) can be used as the model space (Fiandaca *et al.* 2018a). The main advantage of this approach is that K is an actual inversion parameter, and therefore the results can be interpreted in terms of hydraulic properties directly. Furthermore, regularization parameters can be defined with respect to K, and sensitivity calculations may be performed for this parameter. In addition, prior information given in terms of K can be used to inform the inversion directly (e.g. in the form of a starting model). It was also shown that the new model parameters are actually less correlated with each other than the classical Cole–Cole parameters (Fiandaca *et al.* 2021). The inversion approach has been tested by a synthetic study on a realistic aquifer analogue data set and compared with HT inversion results by Römhild *et al.* (2022a). Furthermore, the procedure has also been applied to field data, and the IP inversion results were in good agreement with K-estimates derived from borehole data, slug tests, and grain size analysis (Martin *et al.* 2021; Thalund-Hansen *et al.* 2023), thereby demonstrating that the IP-K inversion approach indeed has the potential to map spatial heterogeneities of the hydraulic properties.

However, the petrophysical relations used within this inversion (Revil *et al.* 2012; Weller *et al.* 2015) are derived from laboratory experiments performed on a small set of samples, which is often not representative for the actual field case. Therefore, the accuracy of the K-estimates may be limited due to the inherent uncertainty of the petrophysical approximations. Furthermore, the accuracy of the K-quantification might be affected by the regularization parameters of the inversion. These limitations motivate the idea of incorporating reliable hydraulic data into the IP inversion.

Based on the complementary abilities of HT and IP regarding sensitivity, spatial resolution, and reliability of the K-estimates, the aim of this work is to combine the IP-K inversion approach with a HT traveltime inversion in order to image the distribution of K with high accuracy. In an earlier attempt, the IP results have been calibrated by using hydraulic data providing reliable estimates for an effective hydraulic conductivity K_{eff} (Römhild *et al.* 2022a). However, these calibration techniques are often not straightforward and require a certain amount of manual fitting. Therefore, the objective of this paper is to introduce a joint inversion procedure, in which HT and IP data can be inverted simultaneously for a distribution of K that minimizes both data misfits. Generally, petrophysical joint inversion approaches have already been used in other contexts, such as permafrost sites (Mollaret *et al.* 2020), gas hydrate systems (Turco *et al.* 2021) or reservoir characterization (Gao *et al.* 2012). The inversion strategy presented in this paper aims to combine the high-resolution structural information from IP with the robust K-estimates derived from HT, as well as the complementary sensitivities of both methods to areas of enhanced or reduced K. We implement the joint inversion procedure for a simple synthetic test case to show the main benefits as well as the limitations of the method. In particular, biased petrophysical relations are introduced to assess the robustness of the joint inversion against these uncertainties, compared to individual inversion. The quality of the inversion results is evaluated by using the structural similarity index (SSIM).

The paper is structured as follows. We introduce the two individual inversion strategies for IP and HT as well as the joint inversion approach in Section 2. Subsequently, the individual and joint inversion results based on a synthetic model are presented in Section 3, with special emphasis on the ability of the joint inversion to correct a petrophysical bias within the IP-based K-estimates. We discuss our findings in Section 4, thereby focusing on the applicability to actual field cases. Some concluding remarks as well as an outlook to further research questions are given in the last section.

2 METHODS

2.1 Induced polarization

2.1.1 Petrophysical foundation

The concept of inverting IP data for hydraulic conductivity K is based on the fact that electrical and hydraulic rock parameters are typically governed by the same pore space properties (Slater 2007). In general, the electrical conductivity σ^* of a porous medium can be considered as a frequency-dependent and complex-valued quantity (Vinegar & Waxman 1984):

$$\sigma^*(\omega) = \sigma_{\text{el}} + \sigma^*_{\text{int}}(\omega), \tag{1}$$

which is a superposition of electrolytic conductivity σ_{el} and interface conductivity σ^*_{int}, with $\omega = 2\pi f$ being the angular frequency, and the * denoting complex quantities. It may either be given in terms of real and imaginary part (σ' and σ'', respectively) or as magnitude $|\sigma^*|$ and phase angle ϕ:

$$\sigma^*(\omega) = \sigma'(\omega) + \mathrm{i}\,\sigma''(\omega) = |\sigma^*| \cdot e^{\mathrm{i}\phi}, \tag{2}$$

with i denoting the imaginary unit. The electrolytic part describes the DC conduction through a rock's pore space, and therefore depends on pore volume properties as described by Archie's law

(Archie 1942) assuming fully saturated conditions:

$$\sigma_{\mathrm{el}} = \frac{\sigma_w}{F} = \Phi^m \cdot \sigma_w, \tag{3}$$

where σ_w is the pore water conductivity, $F = \Phi^{-m}$ is the formation factor, Φ is porosity, and m is the empirical cementation exponent.

In contrast, the interface conductivity σ^*_{int} can be governed by a variety of different electrical polarization phenomena mainly attributed to the interface between pore space and rock matrix. In the absence of electronically conductive minerals, such as graphite or pyrite, diffusion-related polarization connected to the electrical double layer (EDL) at the pore–matrix interface is dominant (Marshall & Madden 1959; Schwarz 1962; Olhoeft 1985; Bücker & Hördt 2013). Since these polarization effects strongly depend on the frequency of the applied current, the spectral behavior of σ^* must be taken into account, which is commonly described by the Cole–Cole model (Cole & Cole 1941; Pelton *et al.* 1978; Tarasov & Titov 2013):

$$\sigma^*(\omega) = \sigma_0 \left[1 + \frac{m_0}{1 - m_0}\left(1 - \frac{1}{1 + (\mathrm{i}\omega\tau_\sigma)^c}\right)\right]. \tag{4}$$

Here, σ_0 is the DC conductivity, m_0 the intrinsic chargeability as defined by Seigel (1959), τ_σ the relaxation time, and c the frequency exponent.

In order to achieve the reparametrization of the Cole–Cole model in terms of hydraulic properties, two different petrophysical approaches are applied within this work. First, Weller *et al.* (2015) found a relation to estimate the permeability k that is based on the formation factor F as a measure for the volumetric properties of the pore space, and the imaginary part of the electrical conductivity σ'' evaluated at 1 Hz accounting for the polarization strength:

$$k = \frac{1.08 \cdot 10^{-13}}{F^{1.12}\,(\sigma''(1\ \mathrm{Hz}))^{2.27}} \tag{5}$$

for unconsolidated and fully saturated sediments. Within this approach, the relationship

$$\sigma''(1\ \mathrm{Hz}) = 0.042 \cdot \sigma'_{\mathrm{int}}(1\ \mathrm{Hz}) \tag{6}$$

between imaginary and real part of surface conductivity found by Weller *et al.* (2013) is also used. However, in this work, the relation is imposed at the frequency $f = (2\pi\tau_\sigma)^{-1}$ according to Fiandaca *et al.* (2018b).

As a second approach, we use an equation suggested by Revil *et al.* (2012) using the formation factor F, the diffusion coefficient of the Stern layer D_+, and the relaxation time τ_σ:

$$k = \frac{\tau_\sigma D_+}{4F}. \tag{7}$$

The relation is based on the concept of τ_σ being a measure for typical scale lengths in the rock's pore space, which in return govern hydraulic conductivity. We use the two distinct D_+-values for sand and clay:

$$\begin{aligned} D_{+,\mathrm{sand}} &= 1.3 \cdot 10^{-9} \cdot \mathrm{m^2\,s^{-1}}, \\ D_{+,\mathrm{clay}} &= 3.8 \cdot 10^{-12} \cdot \mathrm{m^2\,s^{-1}}, \end{aligned} \tag{8}$$

given by Revil *et al.* (2015), in order to simulate realistic τ_σ-values within the forward modelling. However, the physical significance of D_+ remains ambiguous (Weller *et al.* 2016), and therefore this parameter might introduce a high degree of uncertainty to this relation (eq. 7). For a more detailed discussion on the inherent limitations of the petrophysical relations, we also refer to Fiandaca *et al.* (2018b) and Römhild *et al.* (2022a).

In order to include different petrophysical approaches within our inversion procedure, both Equations (5) and (7) are used simultaneously, forcing the inversion to produce K-values that fulfil the two relations equally well. This is based on the hypothesis that a combined approach has the potential to make the K-estimation more robust against varying field conditions that may differ from the underlying assumptions of the individual petrophysical relations.

Finally, the conversion from permeability k to hydraulic conductivity K is performed using the relation

$$K = \frac{d \cdot g}{\eta} \cdot k \approx 7.5 \cdot 10^6 \cdot k, \tag{9}$$

where d is the density of the pore fluid, g the gravitational acceleration, and η the dynamic viscosity of the pore fluid. The approximation is achieved by assuming a groundwater temperature of 10 °C.

2.1.2 IP forward modelling

Generally, IP experiments can be conducted either in the frequency domain (spectral induced polarization, SIP) or in the time domain (TDIP). Both approaches can potentially produce consistent results of similar quality (Martin *et al.* 2020). In this work, we focus on TDIP, since it is more widely used within field applications due to a typically smaller acquisition time (Maurya *et al.* 2018b). By performing full-decay spectral inversion (Fiandaca *et al.* 2012, 2013; Madsen *et al.* 2020), an accurate retrieval of spectral properties can be achieved, given that a wide time range is used during data acquisition (Madsen *et al.* 2017), for instance through the analysis of full-waveform recordings (Olsson *et al.* 2016). The general concept of time-domain IP experiments is illustrated in Fig. 1. For more details about the method we refer to Binley & Slater (2020).

The forward response is computed using the WhyCDF model space, similar to Römhild *et al.* (2022a). We assume a constant water conductivity of $\sigma_w = 50$ mS m^{-1} as well as a homogeneous formation factor of $F = 5$ as realistic values for unconsolidated sediments (Schön 2015). The K-distribution is set up according to the synthetic test case given in subsequent Section 2.4, and the diffusion coefficient D_+ is derived from K by interpolation in log-space from the sand-clay values suggested by Revil *et al.* (2015) (eq. 8). Although a continuous relationship between K and D_+ has not yet been proven by other studies, we consider it a reasonable approximation for imposing realistic τ_σ-values on the data. The frequency exponent $c = 0.5$ is assumed homogeneous. Clearly, these can be strong assumptions, especially regarding a constant formation factor. However, it was shown in previous works that an accurate K-distribution is also achieved when including spatial variability in F (Römhild *et al.* 2022a). Nevertheless, the synthetic experiments can only be regarded as best-case scenarios that illustrate the general potential of the method.

The specific setup of the IP experiments is given in section 2.4. The forward simulation is executed using EEMverter, an inversion tool for electric and electromagnetic data (Fiandaca *et al.* 2023). The 2-D solution of the forward problem is computed in the frequency domain, and then transformed to the time domain through a Hankel transform taking into account both the current waveform and the receiver transfer function, following Fiandaca *et al.* (2013).

Finally, Gaussian noise of 2 and 10 per cent magnitude is added to resistivity and IP data, respectively. As illustrated in Fig. 1(d), this can be regarded as a relatively high noise level, which accounts for the difficulty to acquire high-quality IP data under certain field conditions. However, we find that decay curves with such noise

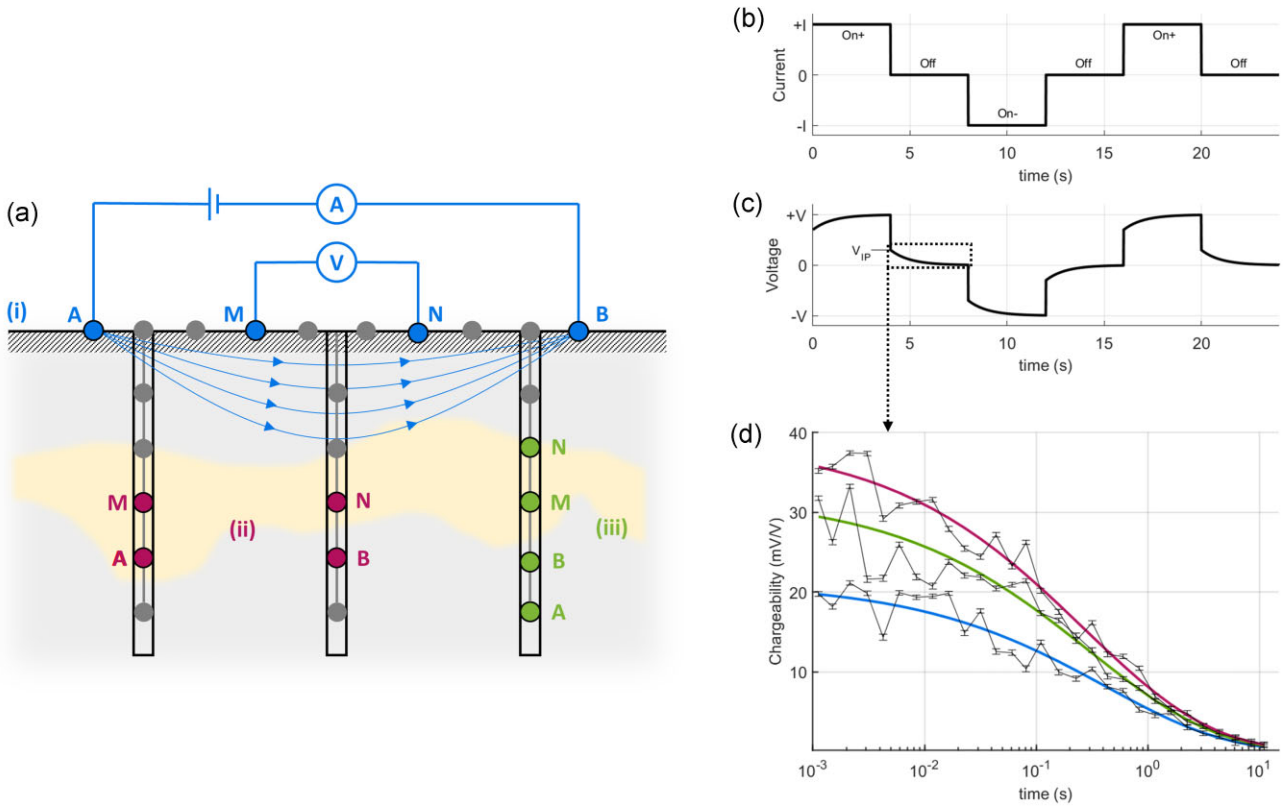

Figure 1. (a) Generalized setup of (i) surface (blue), (ii) cross-borehole (red), and (iii) single-borehole (green) IP experiments with current electrodes A and B, and voltage electrodes M and N. (b) Current signal with alternating on-times and off-times and (c) observed voltage including charging curves and decay curves caused by the polarization effects. (d) Exemplary voltage decay curves with added Gaussian noise (black lines with error bars), and the respective curves fitted by the inversion (coloured lines).

content can still be fitted by the inversion, so that the approach can be expected to be applicable to field data.

2.2 Hydraulic tomography

2.2.1 Full modelling

The HT experiments are simulated by using the finite element solver of pyGIMLi, a Python-based open-source library for multimethod modelling and inversion in geophysics (Rücker *et al.* 2017). The geometries of the test cases and the corresponding mesh are generated by the submodule 'meshtools', and the K-information of the synthetic model (see Section 2.4) is assigned to the different layers.

Flow in the porous medium, modelled as a continuum, is governed by Darcy's law and the continuity equation. Therefore, the governing equation of the simulation is the following partial differential equation (PDE):

$$S_s \frac{\partial h}{\partial t} - \nabla \cdot (K \nabla h) = 0, \tag{10}$$

which can also be written as

$$S_s \frac{\partial h}{\partial t} - \nabla K \cdot \nabla h - K \nabla^2 h = 0. \tag{11}$$

In both formulations, S_s is the specific storage, K is the hydraulic conductivity, and h is the hydraulic head. Eq. (10) can be implemented using the function 'solveFiniteElements' of pyGIMLi, which solves PDEs matching the form

$$c \frac{\partial u}{\partial t} = \nabla \cdot (a \nabla u) + bu + f(\mathbf{r}, t), \tag{12}$$

by setting $u = h$, $a = K$, $b = 0$, $c = S_s$, and $f = 0$. The hydraulic head on the sides of the domain is kept at zero by applying a Dirichlet boundary condition. The injection is implemented as a Neumann boundary condition applied to the respective injection intervals. Examples of the full solution of the PDE (eq. 10) are shown in Fig. 2(b), where the pressure response curves (hydraulic head over time, in response to a Heaviside pumping signal) are plotted for different combinations of source receiver pairs. This full modelling approach is applied for computing the synthetic HT data used in this work. However, only the peak times of the head responses (the times at which the first derivatives of the pressure signals reach their maximum) are used as data in the inversion process, as explained in the subsequent section. The specific setup for the experiments shown in this work is given in Section 2.4.

2.2.2 Traveltime approximation

For computing the forward response within the inversion of HT data, we use the traveltime approximation of eq. (11), which neglects the $(\nabla K \cdot \nabla h)$ term in comparison to $S_s \frac{\partial h}{\partial t}$, such that the peak time (or the time for reaching a fraction α of the peak) can be computed as the line integral between the source point S_i (where the pumping-induced pressure is generated) and the receiver point R_i (where the resulting hydraulic head is observed), following the ray path ε:

$$\sqrt{t_{\alpha,h}} = \frac{1}{\sqrt{6 f_{\alpha,h}}} \int_{S_i}^{R_i} \frac{d\varepsilon}{\sqrt{\frac{S_s(\varepsilon)}{K(\varepsilon)}}}, \tag{13}$$

where $t_{\alpha,h}$ is the time for reaching the fraction α of the peak, and $f_{\alpha,h}$ is a scaling factor that is computed numerically from the diffusion

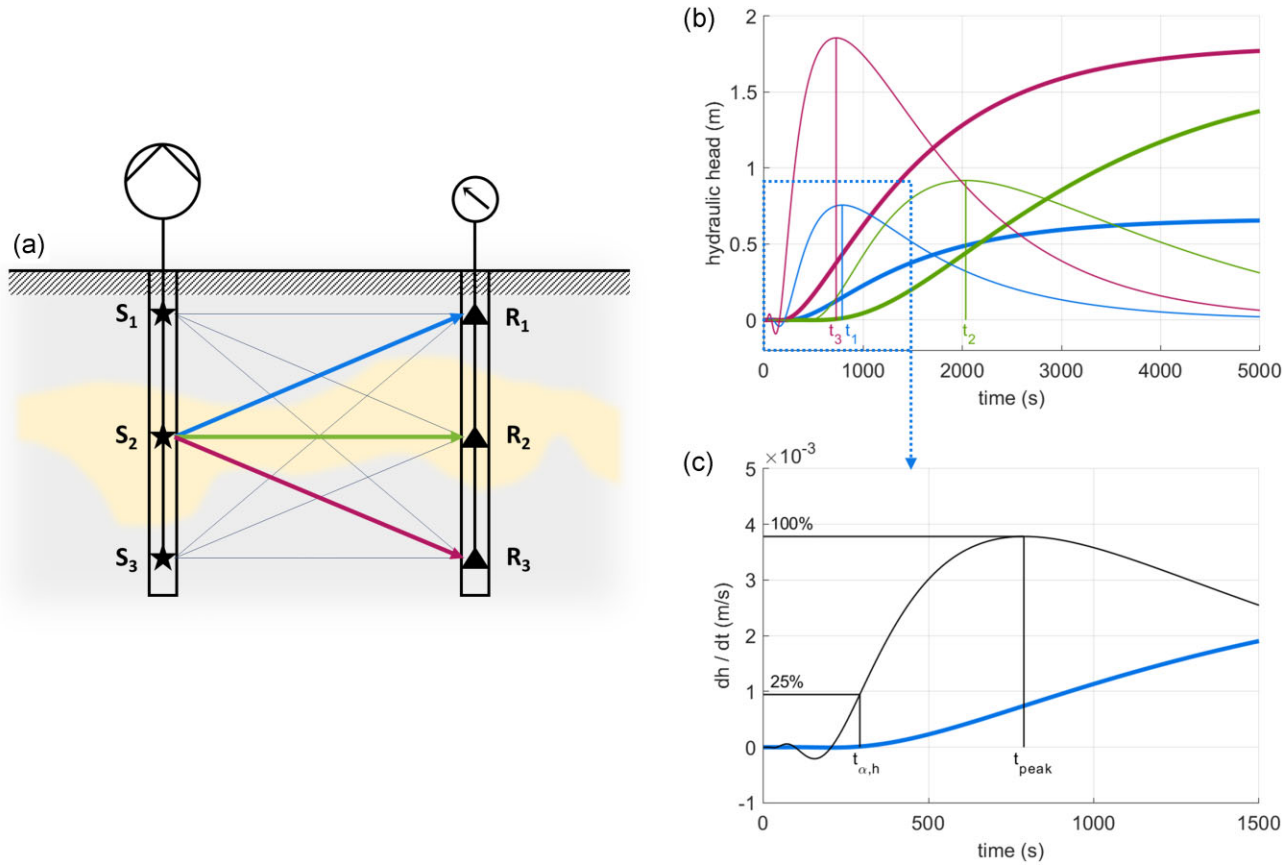

Figure 2. (a) Generalized setup of a HT experiment with simplified ray paths between source points S_i and receiver points R_i. (b) Traveltime processing of HT data. The bold lines represent the hydraulic head response at the receiver points initiated by a Heaviside signal at the pumping locations. The thin lines are the respective first derivatives, and the peak times t_i are picked at the maximum of these curves. The colour-coding refers to the ray paths in (a). (c) Early-time diagnostics for traveltime processing. The bold, blue line is the hydraulic head response of the first ray path, while the thin, black line shows its first derivative. The early time $t_{\alpha,h}$ is picked where the derivative reaches 25 per cent of its maximum value. Note that numerical instabilities commonly occur in the early phase of the pumping experiment simulation.

equation of homogeneous media (Brauchler *et al.* 2003). The subscript $_h$ indicates that a Heaviside signal was used for the pumping tests. In this work, we apply a 25 per cent early time diagnostics approach (i.e. $\alpha = 0.25$) according to Brauchler *et al.* (2003). By using earlier traveltimes, the sensitivity of the inversion to preferential flow paths can be enhanced (Hu 2011). Similar to seismic traveltime inversion (Zelt & Smith 1992), eq. (13) can be solved by using ray tracing techniques. For this purpose, the 'traveltime' submodule of pyGIMLi is utilized for computing the forward response based on Dijkstra's algorithm (Dijkstra 1959). A noise level of 3 per cent was added to the traveltime data, based on Doetsch *et al.* (2010) and Hu *et al.* (2017).

2.3 Inversion

2.3.1 IP-K inversion

The data space of the IP inversion comprises both the DC data and the complete IP decays for the respective quadrupole sequence. The inversion of these data is performed in the ThyCD model space similar to Römhild *et al.* (2022a). Consequently, the inversion parameters comprise the total (DC) conductivity σ_0, the hydraulic conductivity K, the diffusion coefficient D_+, and the frequency exponent c. When evaluating the inversion results, D_+ might also be interpreted in terms of an apparent diffusion coefficient D_a as described by Weller *et al.* (2016). The inverse problem is solved within the EEMverter framework through an iterative Gauss-Newton scheme based on Fiandaca *et al.* (2013, 2023), where the objective function contains the squared data misfit and smoothness regularization terms for vertical and horizontal constraints. The constraints allow for adjusting the spatial variability of each model parameter in horizontal and vertical direction. However, all four model parameters remain uncoupled and space-dependent within the inversion.

2.3.2 HT inversion

The data space of the HT inversion comprises the early times $t_{\alpha,h}$ of the source receiver pairs of the simulated sequence (described in Section 2.4), while the model space is defined by the 2-D distribution of K (assuming homogeneous S_s). Although the inversion could be fully performed in the pyGIMLi environment together with the forward computations, EEMverter is used in this study for carrying out the HT inversions (as well as the joint inversions), thanks to the feature of EEMverter of accepting external forward and jacobian computations. Additional codes for establishing the interface between EEMverter and pyGIMLi are implemented in MATLAB, and the transfer of the data is handled by text-based files. In particular, the model of the current iteration (i.e. the K-distribution) is exported by EEMverter and then used by pyGIMLi for the forward calculation. The resulting HT data (i.e. the traveltimes) as well as the Jacobian matrix for this model are subsequently transferred back to EEMverter, which handles the actual inversion procedure.

2.3.3 Joint inversion

The joint inversion of both data types is also implemented using the EEMverter framework, with internal computation of DC and IP data and external forward calculation of the HT response using pyGIMLi. Generally, the results can be achieved by either a classical, fully joint inversion (minimizing both data misfits simultaneously), or by working with different inversion cycles. In the latter case, the inversion might be performed for one data type only in a first cycle, and the joint inversion of both data sets is executed in a second cycle using the result of the first cycle as a starting model. In this paper, only results from the fully joint, single-cycle inversion are shown to ensure comparability. The use of the same inversion algorithm for all the inversion types in this study (IP-K inversion, HT traveltime inversion, and joint inversion) allows for a fair and easy comparison of inversion results, because regularization, damping, data weighting, and stopping criteria are treated in the same way for all data types.

Since the number of IP data points is typically larger than the available HT data points, considerations about the correct weighting of the different methods within the joint inversion are necessary. In the current form of the algorithm, data are weighted according to their given standard deviation. For the synthetic data used in this work, we have carefully chosen reasonable standard deviation models that ensure a well-balanced influence of the two methods within the joint inversion. However, for the inversion of field data, where the standard deviation is an inherent part of the data that cannot be modified, the implementation of an explicit weighting factor might become necessary.

2.4 Synthetic model

To illustrate the advantages as well as the limitations of the joint inversion approach, a simple synthetic model mimicking horizontally layered sediments with alternating hydraulic conductivity is constructed (Fig. 3a). The model domain has a horizontal extension of 12 m and extends down to 8 m depth. It primarily consists of material with an intermediate hydraulic conductivity of $K = 10^{-6}\,\mathrm{m\,s^{-1}}$, intermitted by a layer of 1 m thickness with high hydraulic conductivity ($K = 10^{-4}\,\mathrm{m\,s^{-1}}$) at 2 m depth, another layer of the same thickness with low hydraulic conductivity ($K = 10^{-8}\,\mathrm{m\,s^{-1}}$) at 4 m depth, and a thinner layer (0.5 m) of high hydraulic conductivity ($K = 10^{-4}\,\mathrm{m\,s^{-1}}$) at 6 m depth. In this way, the different sensitivities of the two methods for areas of enhanced K (HT) or reduced K (IP) shall be illustrated. In addition, the ability of the different experimental setups to resolve small-scale structural features, such as thin horizontal layers, shall be assessed.

While the hydraulic conductivity is the shared parameter used within the synthetic experiments of both HT and IP, the model also comprises additional parameters that are individually required for one of the methods. The underlying assumptions for those parameters are described in the respective sections about the synthetic experiments (Sections 2.2.1 and 2.1.2), while the values used in the simulations are shown in Fig. 3, including the diffusion coefficient D_+ (Fig. 3b). To illustrate the effect of the heterogeneity in K and D_+ on the IP response, additional electrical parameters are shown in Figs 3c–f. Note that those are not defined as model parameters but can be derived from the other parameters by using the petrophysical conversions given in Section 2.1.1. Consequently, smaller values for K lead to a stronger polarization (manifested as higher phase peak $\phi_{\max}$ and higher σ''), shorter relaxation times τ_σ, and a higher DC conductivity σ_0.

In all cases, it is assumed that three boreholes are located in the model domain with a horizontal distance of 3 m and a vertical extension down to 7 m depth. The electrodes for the IP experiments as well as pumping and observation locations of the HT setup are placed in those boreholes.

For the HT experiments, the injection intervals are located in the left borehole at $x = 3\,\mathrm{m}$. We use an interval length of 0.1 m and an injection rate of $0.5\,\mathrm{m\,s^{-1}}$ to simulate pumping tests, which are conducted sequentially from top to bottom. The observation points are located in two other boreholes at $x = 6\,\mathrm{m}$ and $x = 9\,\mathrm{m}$ at the same depths as the injection intervals, and the hydraulic head is recorded over time at the nearest node of the mesh.

The setup of the IP data acquisition is based on a common cross-borehole scheme with electrodes being distributed with 25 cm spacing in the three hypothetical boreholes at $x = 3$, 6 and 9 m. Note that for this study no surface electrodes are used to allow a fair comparison with the HT experiments. The sequence is built using a combination of cross-borehole and single-borehole quadrupoles [cases (ii) and (iii) in Fig. 1a, similar to Römhild *et al.* (2022a)], consisting of 1860 quadrupoles in total. Each decay curve is defined by 41 IP time gates ranging from 0.003 to 12 s (Fig. 1c).

3 INVERSION RESULTS

3.1 Individual HT and IP inversion results

The K-images resulting from the different test cases are shown in Fig. 4 in comparison with the synthetic model (a). In the IP result (Fig. 4b), the different layers of the model are reproduced by the inversion and the overall K-quantification is accurate. A high spatial resolution can be achieved due to the small electrode spacing of 25 cm. However, regularization-induced smoothing effects lead to a tendency of underestimating K in the high-permeability zones and overestimating K in the less permeable areas. The limited ability to correctly reproduce sharp boundaries and strong parameter contrasts is a common characteristic of inversion procedures using smoothness constraints (Loke *et al.* 2003). In particular, the thin layer of high K at 6 m depth is strongly underestimated, which is also a result of the reduced sensitivity of IP to high-K zones due to the weakness of the polarization effects. However, such thin layers of enhanced K often serve as major flow paths within an aquifer and are therefore important to capture.

For the HT inversion, we show three different inversion results for different experimental setups: (i) with 1 m spacing between the pumping locations as well as between the receiver points (Fig. 4c, data set with 98 traveltimes), (ii) with 2 m spacing, and points being placed inside the layers (Fig. 4d, data set with 18 traveltimes), and (iii) with 2 m spacing, and points being placed outside the layers (all points in areas of $K = 10^{-6}\,\mathrm{m\,s^{-1}}$, Fig. 4e, data set with 32 traveltimes). In the first case, the two layers of high K are clearly visible in the results, since they serve as preferential flow paths during the HT experiments. The low-K layer has also been reproduced by the inversion due to acting as a hydraulic barrier between some of the source receiver pairs. Generally, although the K-quantification in terms of average values is accurate, the spatial resolution of the result is much lower compared to IP due to the larger spacing between the source and receiver locations. For the hydraulic experiments, a spacing smaller than 1 m is hardly feasible in practice. Instead, even this setup can be very time-consuming and expensive, and an experiment with even less source and receiver points might be favourable. In this case, when increasing the spacing to 2 m, the individual layer

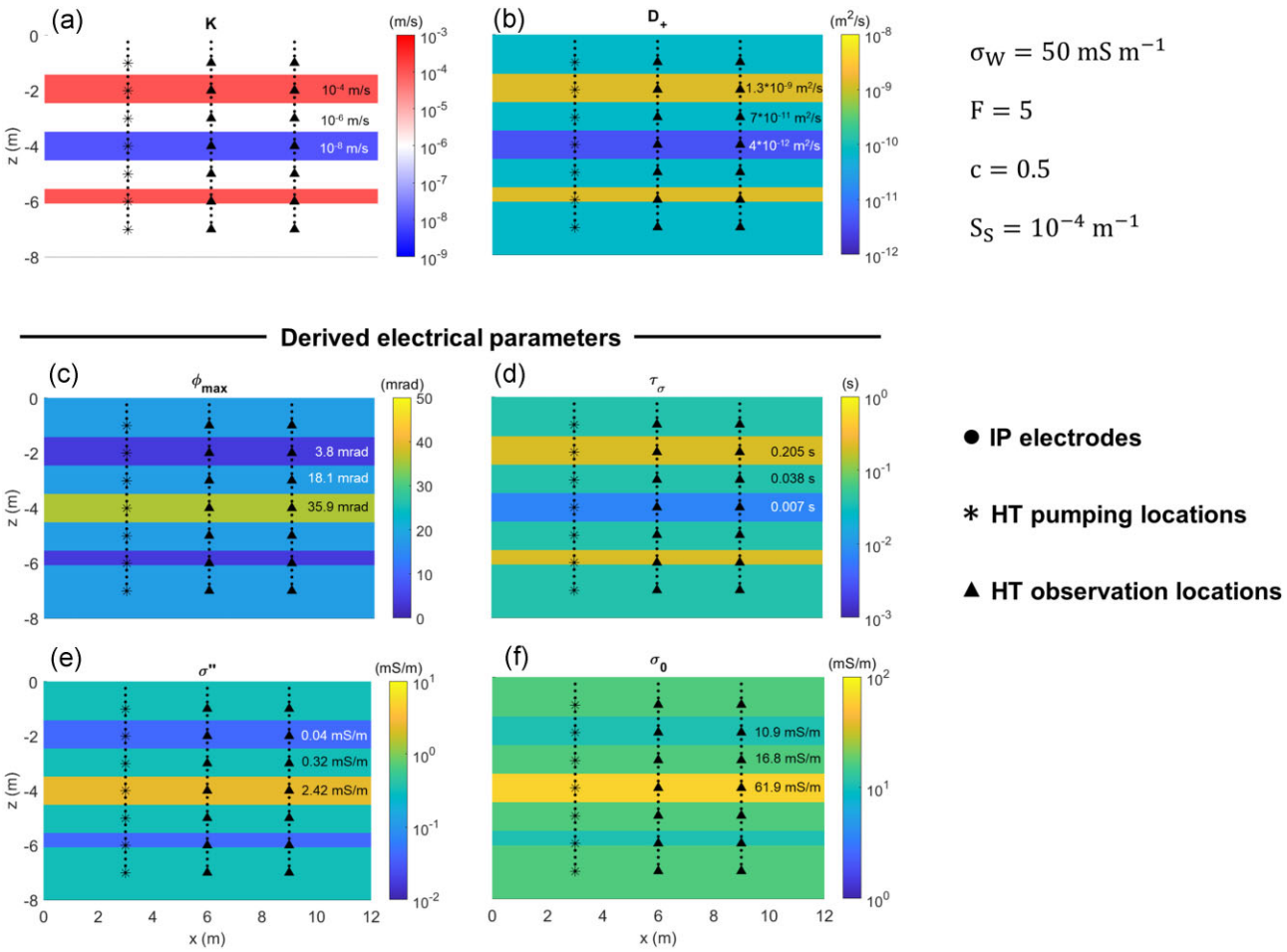

Figure 3. Distribution of hydraulic conductivity K (a) and diffusion coefficient D_+ (b) in the synthetic model. The parameters given on the right are assumed constant for the synthetic experiments. The given parameter set can be used to compute other electrical parameters by the conversions given in Section 2.1.1. Here, we show the maximum phase angle $\phi_{\max}$ (c), the Cole–Cole relaxation time τ_σ (d), the imaginary part of electrical conductivity σ'' evaluated at $f = (2\pi\tau_\sigma)^{-1}$ (e), and the DC conductivity σ_0 (f). Three boreholes are placed at $x = 3$, 6 and 9 m, with IP electrodes (black dots) distributed with 25 cm spacing, and HT source points (asterisks) and receiver points (triangles) with at least 1 m spacing.

boundaries are not well-resolved, and the K-information from the zones of high sensitivity (i.e. the ray paths, which are predominantly inside the layers) migrates to the areas of low sensitivity due to the smoothness constraints. Therefore, large areas of high K and low K are visible in the inversion result, instead of the thin layers from the input model. In the third case (Fig. 4e), where the source and receiver points are placed outside the layers, the inversion result is more dominated by the intermediate K-estimates, and the contrast in K is less pronounced. Furthermore, layer boundaries in the inversion result are shifted towards the modified source and receiver locations, which highlights the strong influence of the sensitivity distribution of the individual experimental setup on the inversion results. Generally, an HT setup with 2 m spacing is not sufficient to resolve the small-scale structural elements of the synthetic model.

3.2 Joint inversion results

The results of the joint inversion are shown in the right section of Figs 4f–h. Clearly, the complementary sensitivities of both methods are combined, so that both high-K and low-K layers can be identified in the results, and their delineation with respect to the areas with intermediate K is more accurate. Furthermore, the high spatial resolution of IP that allows resolving thin layers of contrasting K is complemented by the strong sensitivity of HT to the preferential flow paths, so that the thin layer of high K at 6 m depth is more pronounced than in the individual IP results. Generally, the quantitative estimates of K are very accurate (with stronger contrasts compared to the individual IP inversion) and the joint inversion is more successful in attributing the K-information to the correct location due to being less constraint- and more data-driven. Note that in this case the same smoothness constraints are applied for all inversions to ensure comparability, although it can be beneficial to use different constraints depending on the different methods and setups. In addition, the joint inversion results for the different HT setups are actually very similar, indicating that the joint inversion is more robust against changes in the experimental setup. Even a small amount of pumping tests can be sufficient to extract the relevant information that improve the reproduction of the K-distribution.

3.3 Influence of petrophysical bias

To assess the potential of the joint inversion to correct a bias in the petrophysical relations used within the IP inversion, we now include such bias directly in the forward modelling of the IP data. This is achieved by multiplying the K-values of the synthetic model with a constant factor (10^{-2}, 10^{-1}, 10^{1} or 10^{2}). Therefore, we can only

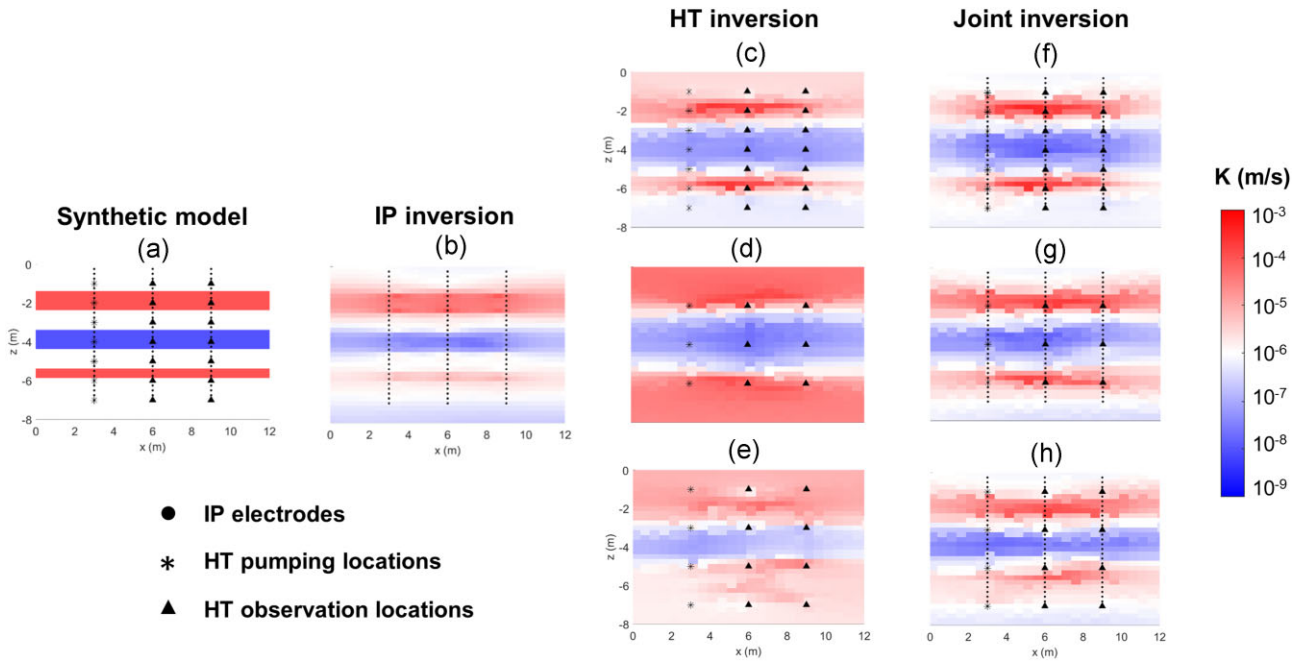

Figure 4. Individual inversion results for IP (b) and HT (c–e), as well as joint inversion results (f–h) in comparison with the original synthetic model (a). In the result plots, only the electrodes/source and receiver points that are contained in the respective data set used for the inversion are shown. The colour bar for K applies to all plots.

account for a constant shift within the petrophysical relations, but not for inherent scatter. All other direct input parameters (including D_+) remain untouched within this modified example. However, note that the electrical properties do change as a result of this modification, similar to the illustrations in Figs 3c–f.

The resulting K-images of the IP inversion are shown in Fig. 5 in the uppermost row of plots. Here, the centre plot depicts the unbiased results as shown in Fig. 4b, the left plots include a negative bias, and the right plots a positive bias of one or two orders of magnitude. As expected, the changes are clearly reflected in the individual IP inversion results, with K being underestimated for the negative bias, and overestimated for the positive bias. In addition, the reproduction of structural features is generally less successful for a stronger petrophysical bias.

Subsequently, the joint inversion is performed for all possible combinations of IP bias and HT setup. The individual HT results are shown again in the left-hand column of Fig. 5—these plots, as well as the joint inversion results without petrophysical bias, are the same as in Figs 4c–e and 4f–h, respectively. For the first two HT setups (1 m, and 2 m inside), the joint inversion is able to reproduce all layers of the synthetic model, with fairly good K-estimates and strong contrasts between the different structural elements. These structures have not been captured by neither the HT inversion nor the biased IP inversion in such detail, but by combining the sensitivities of both methods, a large improvement in the quality of the inversion results is achieved. While HT has the ability to capture the major flow paths (red layers in the plot) and ensures the reliability of the K-quantification, the IP data still contain valuable information about small-scale structural features, even if they are not visible in the individual IP results when assuming a petrophysical bias. For these two cases, the joint inversion results are also robust against changes in the setup of the HT experiments, indicating that reducing the amount of pumping tests is not necessarily problematic. However, when shifting the HT source and receiver location to areas between the layers (last row of plots), the joint inversion results are significantly less accurate. Here, the hydraulic information provided by the HT experiments is not sufficient to correct the petrophysical bias with the same reliability compared to the first two setups. This indicates that not only the spacing between HT source and receiver points, but also their exact location with respect to the relevant structural features is crucial for achieving good joint inversion results. Although the second HT setup contains only three pumping tests, the results are significantly better than the third HT setup with four pumping tests. However, compared to the individual IP and HT results, all joint inversion bring improvement to the reproduction of the structural features.

3.4 Comparison of structural similarity

To allow for a more quantitative comparison of the methods, the structural similarity index (SSIM) of the inversion results compared to the synthetic model is calculated. Being rooted in image processing, the SSIM measures the similarity between two images by considering luminance, contrast, and structural information (Wang *et al.* 2004), and is bounded from 0 to 1, while the latter value indicates perfect similarity between two images. The index has already been used as a tool for assessing the quality of geophysical inversion results (e.g. Giraud *et al.* 2018; Almadani *et al.* 2021; Römhild *et al.* 2022a), or for quantifying the prediction quality of machine learning approaches (Thibaut *et al.* 2021). In our work, the Python package 'scikit-image' (van der Walt *et al.* 2014) is utilized for calculating the SSIM, and only the part of the domain between the boreholes is used for the computation, since the sensitivity of HT is restricted to this area.

The results are shown in Fig. 6 with respect to the petrophysical bias applied to the IP data. For the individual IP inversion (black curve with triangular markers), the SSIM is approximately 0.46 for the unbiased case, and decreases significantly for the negative bias of one order of magnitude (0.14), and two orders of magnitude (0.01).

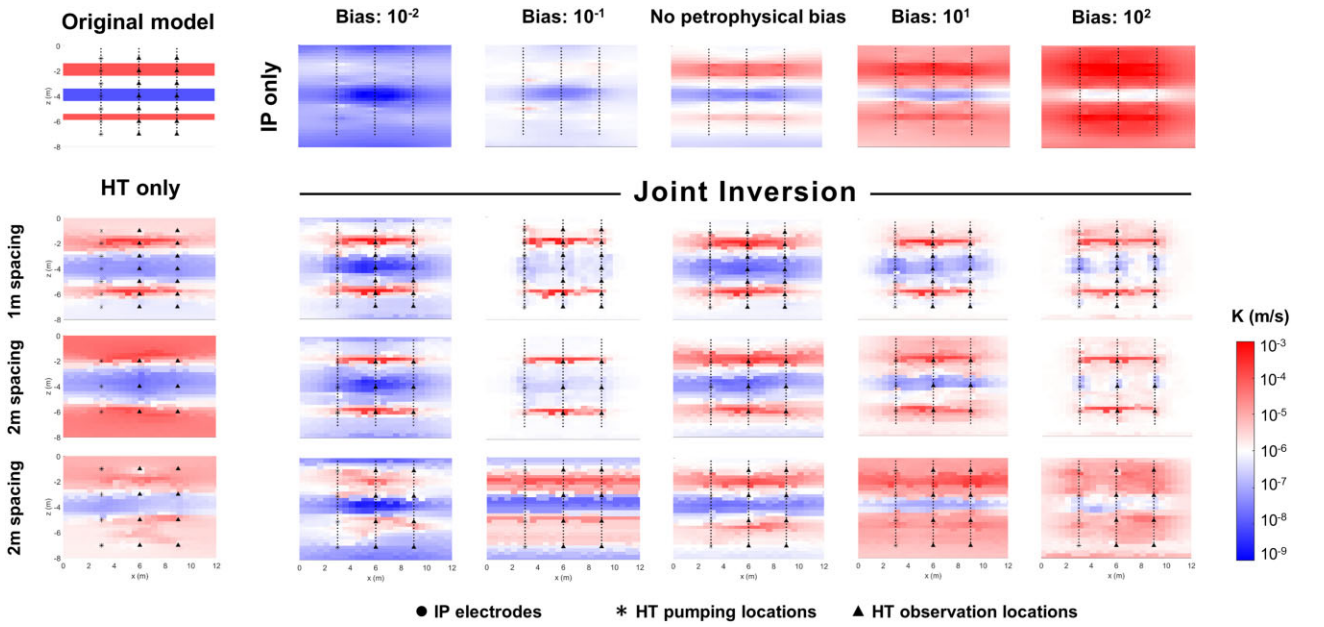

Figure 5. Inversion results for the individual HT inversion (left column), the individual IP inversion including petrophysical bias factors (uppermost row), and joint inversion results for all possible combinations. The colour bar for K applies to all plots.

As shown above, the structural features of the model can hardly be reproduced when assuming a negative petrophysical bias (Fig. 5). In contrast, a positive bias of one order of magnitude actually produces the highest SSIM (0.58). Apparently, due to the limited sensitivity of IP to high-K areas, the inversion result is improved when the K-prediction is shifted by a certain factor. As shown in Fig. 5, the contrast between the different layers is more pronounced for the 10^1-bias compared to the unbiased result, and the K-prediction in the highly permeable layers is more accurate. This is also in accordance with some findings by Römhild *et al.* (2022a), where calibrating the IP results with a constant K_{eff} derived from hydraulic tests ('factor calibration') was found to be a helpful approach for improving the results of transport simulations. However, when increasing the bias even further to two orders of magnitude, the quality of the results is significantly reduced, characterized by an SSIM of 0.06. Generally, the individual IP results show a strong dependency on a potential bias of the petrophysical relations, which is not only influenced by the amplitude, but also the direction of the bias.

The SSIM of the individual HT results is visualized by circle markers, with the colours indicating the different setups. While the setup with 1 m spacing (blue) produces an SSIM of 0.57, which is slightly higher than the individual IP inversion, a setup with larger spacing (2 m) results in a poorer reproduction of the structural features and K-estimates, with an SSIM of 0.32 for source and receiver points inside the layers (red), and an SSIM of 0.16 for points outside the layers (green). This is in accordance with the visual inspection of Figs 4 and 5. The quality of the individual HT inversion results strongly depends on the specific setup of the hydraulic experiments, and a sufficiently small spacing of source and receiver points (i.e. a large number of time-consuming pumping tests) has to be used to achieve results that have a similar quality compared to IP.

The SSIM of the joint inversion results is shown by asterisk markers, and the colours indicate the setup of the used HT data. When using the unbiased IP data within the joint inversion, significantly higher SSIM values can be achieved compared to the individual HT inversion, for all three HT setups (compare pairs of circle and asterisk markers of the same colours in the plot). Compared to the unbiased IP result, the SSIM values of the joint inversion are also slightly higher for all three HT setups, indicating an improved inversion result even when only sparse hydraulic data are used to complement the IP data.

When including the biased IP data in the joint inversion, most of the resulting SSIM values are still higher than the respective individual HT values (or at least in a similar range). It shows that complementing hydraulic tests by IP experiments can even be beneficial when the underlying petrophysical assumptions are not entirely fulfiled at the specific field site. In any case, the high-resolution structural information from the IP data is valuable, and it is worth including them in the joint inversion procedure, even if the exact quantification of K by the IP experiments is not correct.

When comparing the joint inversion results with the individual IP results, significantly higher SSIM values can be observed in nearly all cases. The only exception for this specific model is the 10^1-bias, where the individual IP inversion had produced an exceptionally high SSIM value, as explained above. Here, the SSIM values of the joint inversion are slightly smaller, but still indicate a high quality of the inversion results.

The joint inversion results using the first two HT setups (blue and red markers in Fig. 6) are particularly robust against the petrophysical bias of the IP data. Here, the SSIM values of the biased joint inversion results are almost as high as for the unbiased joint inversion result (roughly between 0.4 and 0.6). This indicates that by using the reliable K-estimates from the hydraulic tests, the bias of IP resulting from the uncertainty of the petrophysical relations can indeed be corrected. However, a suitable HT setup is crucial for achieving such significant improvements. When using the last HT setup (2 m spacing, points outside the layers) for the joint inversion (green markers in Fig. 6), the improvement compared to the individual inversion results is rather modest. If the HT source and receiver positions are placed outside the relevant structural features, the hydraulic information is less valuable for the joint inversion procedure. Therefore, the exact location of the source and receiver points can in

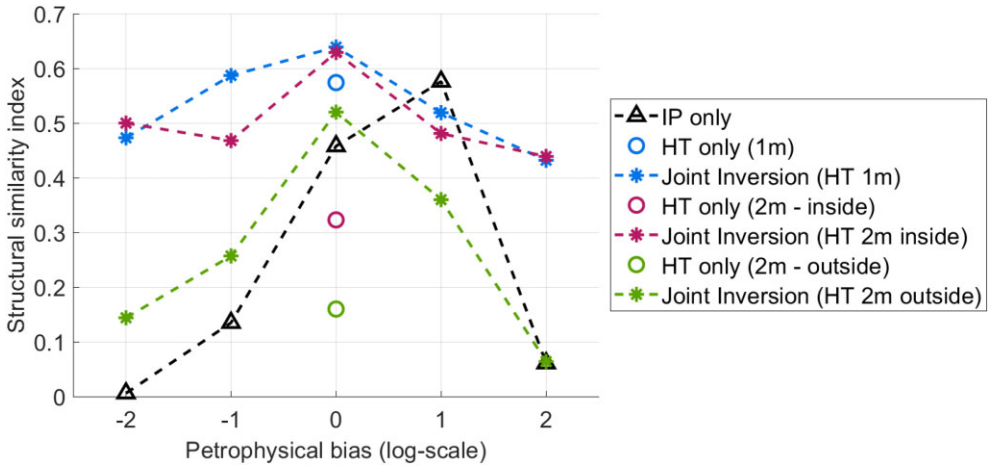

Figure 6. Structural similarity index (SSIM) of the inversion results, compared to the original synthetic model, for the different inversion methods, and with varying petrophysical bias. The dashed lines are for visual guidance only.

some cases be more important than simply the amount of pumping tests.

4 DISCUSSION

The main objective of the presented methodology is the correction of potential petrophysical uncertainties within the IP-K inversion, as presented in the previous section. Those uncertainties may arise, for instance, from the empirical parameters in the approach of Weller *et al.* (2015), or from the limited applicability of the diffusion coefficient D_+ in the relation of Revil *et al.* (2012). The latter may also be interpreted as an apparent diffusion coefficient D_a in the inversion results (Weller *et al.* 2016), but its physical significance in the context of IP inversion remains ambiguous. In addition, petrophysical relations are also resolution-dependent, and may not hold on different scales (Singha *et al.* 2015; Hermans & Irving 2017). They are mostly derived from a relatively small set of samples in the laboratory, which is often not representative for the actual field conditions (e.g. Benoit *et al.* 2019).

To overcome these problems, the idea of jointly evaluating electrical and hydraulic data has already been proposed by Slater (2007). We have now shown that a joint inversion of HT and IP data is a promising approach for implementing this concept. Including the reliable K-estimates from the hydraulic data can potentially correct a petrophysical bias within the IP inversion, thereby overcoming some of the aforementioned uncertainties.

The presented inversion approach relies on a single-component Cole–Cole model, which can be seen both as an oversimplification or as an unnecessary complexity, depending on the point of view. The rationale of this choice is that a frequency-dependent model is necessary for taking into account eq. (7) in the K-estimation, and that the Cole–Cole model is widely used for fitting IP spectra of data acquired in the field and consequently for parametrizing the model space of IP inversions. However, some sediments may not show a single-component polarization peak, but are instead characterized by several polarization components at different frequencies (Weigand & Kemna 2016; Römhild *et al.* 2022b): in these cases, a more complex description of the electrical properties and of the link between electrical and hydraulic properties might be used, for instance in terms of Debye decomposition (Nordsiek & Weller 2008; Zisser *et al.* 2010; Hase *et al.* 2022). On the contrary, when a constant-phase behaviour (Börner *et al.* 1996; Weller *et al.* 1996; Lajaunie *et al.* 2016) is sufficient for describing the electrical properties of the sediments, the proposed approach should still work, since the Cole–Cole model for very small values of the frequency exponent c becomes a constant phase angle model.

For the latter case, a much simpler method of inferring K from IP data has been proposed by Flores Orozco *et al.* (2022). It is based on computing σ'' from the integral chargeability, and then relying on the petrophysical relations of Weller *et al.* (2015) for computing K. However, this approach does not consider the actual spectral characteristics of the data, and variations in spectral content as well as non-standard decay types [e.g. heterodox transients as described by Fiandaca *et al.* (2022)] might lead to bias in the inversions. Instead, a full decay inversion can potentially cover these transient types, and is therefore favourable for inverting cross-borehole IP data.

Another critical point for every geophysical joint inversion is the dimensionality of the problem depending on the acquisition schemes of the different methods (JafarGandomi & Binley 2013; Ghalenoei *et al.* 2022). For a successful joint inversion of all data types, consistent acquisition geometries are crucial. In our test case, the data acquisition points of both HT and IP are placed in the same boreholes, so that the two data sets cover the same 2-D cross-section. Such setups should also be most feasible within field applications. However, the experiments cannot be carried out simultaneously, so it needs to be ensured that temporal changes in the subsurface between the measurements, for instance due to seasonal variations, are negligible.

Furthermore, field measurements could also contain IP data collected on a surface profile. If such profile covers the same cross-section as the boreholes, so that the overall inversion problem is restricted to a 2-D section, the current version of the presented algorithm is still applicable. Although surface IP experiments have a limited ability of resolving small-scale structures in greater depths, the HT data might still cover this depth range, and a joint inversion of both data types would benefit from the complementary sensitivities. If no borehole electrodes are installed, simultaneously carrying out both experiments might be practically possible, but the hydraulic stimulation during the HT experiments could strongly affect the resulting IP signal (e.g. due to streaming-induced self-potential). Therefore, a sequential measuring procedure is still advisable.

Challenges for the joint inversion of HT and IP data might arise from strongly differing geometries, especially if the combined data set is not restricted to a 2-D cross section but covers a 3-D domain. Currently, the inversion algorithm presented here is not available for 3-D applications, but it will be extended in the future [similar to Madsen *et al.* (2020)]. However, sufficient overlap in the sensitivity coverage would be crucial to ensure that the hydraulic data can potentially correct biased IP-based K-estimates within the joint inversion. For this purpose, pre-experimental synthetic studies investigating the exact sensitivity distributions would be indispensable to optimize the acquisition geometry. Additionally, the computational cost to invert for a 3-D distribution of the model parameters increases drastically, so that high-performance workstations are required. Similar issues would arise from including anisotropy in the model, which is necessary in some geological settings.

5 CONCLUSIONS

In a new attempt of combining geophysical and hydrological approaches for imaging hydraulic conductivity K, IP and HT data were processed together within a fully joint inversion. Thereby, the complementary abilities of both methods regarding sensitivity, spatial resolution and reliability of the K-estimates were combined. We tested the new joint inversion strategy on a simple synthetic test case to illustrate the benefits and limitations of the method. It could be shown that the joint inversion brought significant improvements when comparing the results to the individual IP and HT inversion, especially when hydraulic information is sparse. In addition, the robustness against uncertainties in the petrophysical relations underlying the IP inversion was significantly increased when using the joint inversion approach. By including the HT data, a possible petrophysical bias was successfully corrected by the reliable K-estimates from the hydraulic tests, while the high-resolution structural information from IP is also preserved. Compared to the calibration approaches proposed by Römhild *et al.* (2022a), the joint inversion has the ability of handling the complementary information from the two data sets automatically, is therefore more elegant, and does not require any manual tuning.

However, the present study shall only be regarded as a starting point showing the general potential of the joint inversion approach. In future works, the methodology can be tested on more complex synthetic models, like aquifer analogue data sets similar to Heinz *et al.* (2003) or Bayer *et al.* (2015), also assessing the influence of other experimental setups, as well as, potentially, more complex bias in the petrophysical relations of IP. Furthermore, expanding the approach to data sets with different dimensions might be an important step towards fully capturing the hydraulically relevant structures in the subsurface.

Clearly, the application of the joint inversion approach to field data will be crucial to test the actual applicability of the method in practice. For that purpose, a well-known field site should be chosen to enable the comparison with already available stratigraphical and hydraulic information, and ideally with other geophysical data. The applicability of the petrophysical relations needs to be ensured by choosing a site with unconsolidated, fully saturated sediments characterized by significant heterogeneities in the hydraulic parameters. Pre-experimental synthetic studies might be conducted to determine the most suitable setup for imaging the relevant structures. Ultimately, the inversion results could be validated by performing tracer experiments as proposed by Römhild *et al.* (2022a).

Generally, we would like to encourage the combined application of geophysical and hydrological methods in the context of imaging the hydraulic parameters of the near-surface Earth. By applying a joint inversion procedure as proposed in this work, the benefits of two complementary methods can be combined, thereby yielding results with much higher resolution and accuracy. In particular, an improved understanding of the small-scale subsurface heterogeneities in the hydraulic parameters can be essential to achieve more reliable predictions from flow and transport models, which strongly depend on the underlying K-information. Therefore, a joint inversion of IP and HT data can be an important contribution towards the goal of understanding and modelling flow and transport processes in aquifers more correctly.

ACKNOWLEDGMENTS

We would like to thank the reviewers Robin Thibaut and Andreas Weller for their constructive comments that strongly helped to improve the manuscript, and Ryan Pearson for proofreading.

AUTHOR CONTRIBUTIONS

Lukas Römhild (Conceptualization [Equal], Data curation [Equal], Investigation [Equal], Methodology [Equal], Software [Equal], Visualization [Equal], Writing – original draft [Equal]), Gianluca Fiandaca (Conceptualization [Equal], Methodology [Equal], Software [Equal], Supervision [Equal], Writing – review & editing [Equal]), and Peter Bayer (Conceptualization [Equal], Project administration [Equal], Supervision [Equal], Writing – review & editing [Equal]).

DATA AVAILABILITY STATEMENT

The synthetic model and data, as well as all inversion results shown in this work are available through: Römhild, L., Fiandaca, G., & Bayer, P. (2024). Induced polarization and hydraulic tomography joint inversion results on a synthetic model [Data set]. Zenodo. https://doi.org/10.5281/zenodo.10208903.

REFERENCES

Almadani, M., Waheed, U.B., Masood, M. & Chen, Y., 2021. Dictionary learning with convolutional structure for seismic data denoising and interpolation, *Geophysics,* **86**(5), 1SO–Z1.

Archie, G.E., 1942. The electrical resistivity log as an aid in determining some reservoir characteristics, *Trans. Am. Inst. Min., Meallurg. Petrol. Eng.,* **146,** 54–62.

Attwa, M. & Günther, T., 2013. Spectral induced polarization measurements for predicting the hydraulic conductivity in sandy aquifers, *Hydrol. Earth Syst. Sci.,* **17,** 4079–4094.

Bayer, P., Comunian, A., Höyng, D. & Mariethoz, G., 2015. High resolution multi-facies realizations of sedimentary reservoir and aquifer analogs, *Sci. Data,* **2,** doi:10.1038/sdata.2015.33.

Benoit, S., Ghysels, G., Gommers, K., Hermans, T., Nguyen, F. & Huysmans, M., 2019. Characterization of spatially variable riverbed hydraulic conductivity using electrical resistivity tomography and induced polarization, *Hydrogeol. J.,* **27,** 396–407.

Berg, S.J. & Illman, W.A., 2011. Three-dimensional transient hydraulic tomography in a highly heterogeneous glaciofluvial aquifer-aquitard system, *Water Resour. Res.,* **47**(10), W10507.

Berg, S.J. & Illman, W.A., 2013. Field study of subsurface heterogeneity with steady-state hydraulic tomography, *Groundwater,* **51**(1), 29–40.

Binley, A. & Slater, L.D., 2020. *Resistivity and Induced Polarization - Theory and Applications to the Near-Surface Earth,* Cambridge Univ. Press.

Binley, A., Hubbard, S.S., Huisman, J.A., Revil, A., Robinson, D.A., Singha, K. & Slater, L., 2015. The emergence of hydrogeophysics for improved understanding of subsurface processes over multiple scales, *Water Resour. Res.,* **51,** 3837–3866.

Binley, A., Slater, L.D., Fukes, M. & Cassiani, G., 2005. Relationship between spectral induced polarization and hydraulic properties of saturated and unsaturated sandstone, *Water Resour. Res.,* **41**(12), doi:10.1029/2005WR004202.

Bohling, G.C. & Butler, J.J., Jr., 2010. Inherent limitations of hydraulic tomography, *Groundwater,* **48**(6), 809–824.

Börner, F.D., Schopper, J.R. & Weller, A., 1996. Evaluation of transport and storage properties in the soil and groundwater zone from induced polarization measurements, *Geophys. Prospect,* **44,** 583–601.

Brauchler, R., Hu, R., Hu, L., Jiménez, S., Bayer, P., Dietrich, P. & Ptak, T., 2013. Rapid field application of hydraulic tomography for resolving aquifer heterogeneity in unconsolidated sediments, *Water Resour. Res.,* **49**(4), 2013–2024.

Brauchler, R., Liedl, R. & Dietrich, P., 2003. A traveltime based hydraulic tomographic approach, *Water Resour. Res.,* **39**(12), 1370.

Bücker, M. & Hördt, A., 2013. Analytical modelling of membrane polarization with explicit parametrization of pore radii and the electrical double layer, *Geophys. J. Int.,* **194**(2), 804–813.

Cardiff, M., Barrash, W. & Kitanidis, P.K., 2013. Hydraulic conductivity imaging from 3-D transient hydraulic tomography at several pumping/observation densities, *Water Resour. Res.,* **49**(11), 7311–7326.

Cardiff, M., Zhou, Y., Barrash, W. & Kitanidis, P.K., 2019. Aquifer imaging with oscillatory hydraulic tomography: Application at the field scale, *Groundwater,* **58**(5), 710–722.

Cole, K.S. & Cole, R.H., 1941. Dispersion and absorption in dielectrics - I. Alternating current characteristics, *J. Chem. Phys.,* **9,** 341–351.

Comunian, A., Renard, P., Straubhaar, J. & Bayer, P., 2011. Three-dimensional high resolution fluvio-glacial aquifer analog - part 2: geostatistical modeling, *J. Hydrol.,* **405,** 10–23.

Dijkstra, E.W., 1959. A note on two problems in connexion with graphs, *Numer. Math.,* **1**(1), 269–271.

Doetsch, J., Linde, N. & Binley, A., 2010. Structural joint inversion of time-lapse crosshole ERT and GPR traveltime data, *Geophys. Res. Lett.,* **37**(24), L24404.

Fiandaca, G. *et al.*, 2023. Closing the gap between galvanic and inductive methods: Eemverter, a new 1d/2d/3d inversion tool for electric and electromagnetic data with focus on induced polarisation, *Proceedings of the 8th International Airborne Electromagnetics Workshop,* 3–7 September 2023, Fitzroy Island.

Fiandaca, G., Auken, E., Christiansen, A.V. & Gazoty, A., 2012. Time-domain-induced polarization: full-decay forward modeling and 1D lateral constrained inversion of Cole–Cole parameters, *Geophysics,* **77**(3), 213–225.

Fiandaca, G., Madsen, L.M. & Maurya, P.K., 2018a. Re-parameterisations of the Cole–Cole model for improved spectral inversion of induced polarization data, *Near Surf. Geophys.,* **16,** 385–399.

Fiandaca, G., Maurya, P.K., Balbarini, N., Hördt, A., Christiansen, A.V., Foged, N., Bjerg, P.L. & Auken, E., 2018b. Permeability estimation directly from logging-while-drilling induced polarization data, *Water Resour. Res.,* **54**(4), 2851–2870.

Fiandaca, G., Madsen, L.M., Olmo, M., Römhild, L. & Maurya, P., 2021. Inversion of hydraulic conductivity from induced polarisation. Part A: methodology and verification, in *Proceedings of the NSG2021 1st Conference on Hydrogeophysics,* August 2021, Vol. 2021, pp. 1–5, European Association of Geoscientists & Engineers.

Fiandaca, G., Olsson, P.-I., Maurya, P.K., Kühl, A., Bording, T., Dahlin, T. & Auken, E., 2022. Heterodox transients in time-domain-induced polarization, *Geophysics,* **87**(1), E35–E47.

Fiandaca, G., Ramm, J., Binley, A., Gazoty, A., Christiansen, A.V. & Auken, E., 2013. Resolving spectral information from time domain induced polarization data through 2-D inversion, *Geophys. J. Int.,* **192,** 631–646.

Fischer, P., Jardani, A. & Jourde, H., 2020. Hydraulic tomography in coupled discrete-continuum concept to image hydraulic properties of a fractured and Karstified aquifer (Lez Aquifer, France), *Adv. Water Resour.,* **137,** 103523.

Fischer, P., Jardani, A., Wang, X., Jourde, H. & Lecoq, N., 2017. Identifying flow networks in a karstified aquifer by application of the cellular automata–based deterministic inversion method (Lez Aquifer, France), *Water Resour. Res.,* **53**(12), 10 508–10 522.

Flores Orozco, A., Steiner, M., Katona, T., Roser, N., Moser, C., Stumvoll, M.J. & Glade, T., 2022. Application of induced polarization imaging across different scales to understand surface and groundwater flow at the Hofermuehle landslide, *CATENA,* **219,** 106612.

Gao, G., Abubaker, A. & Habashy, T., 2012. Joint petrophysical inversion of electromagnetic and full-waveform seismic data, *Geophysics,* **77**(3), WA3–WA18.

Ghalenoei, E., Dettmer, J., Ali, M.Y. & Kim, J.W., 2022. Trans-dimensional gravity and magnetic joint inversion for 3-D earth models, *Geophys. J. Int.,* **230,** 363–376.

Giraud, J., Lindsay, M., Pakyuz-Charrier, E., Martin, R., Ogarko, V. & Jessell, M., 2018. Impact of uncertain geology in constrained geophysical inversion, *ASEG Extended Abstracts,* **2018**(1), 1–6.

Hase, J., Gurin, G., Titov, K. & Kemna, A., 2022. Conversion of induced polarization data and their uncertainty from time domain to frequency domain using debye decomposition, *Minerals,* **13**(7), 955.

Heinz, J., Kleineidam, S., Teutsch, G. & Aigner, T., 2003. Heterogeneity patterns of Quaternary glaciofluvial gravel bodies (SW-Germany): application to hydrogeology, *Sediment. Geol.,* **158,** 1–23.

Hermans, T. & Irving, J., 2017. Facies discrimination with electrical resistivity tomography using a probabilistic methodology: effect of sensitivity and regularisation, *Near Surf. Geophys.,* **15,** 13–25.

Hördt, A., Druiventak, A., Blaschek, R., Binot, F., Kemna, A., Kreye, P. & Zisser, N., 2009. Case histories of hydraulic conductivity estimation with induced polarization at the field scale, *Near Surf. Geophys.,* **7,** 529–545.

Hu, L., Doetsch, J., Brauchler, R. & Bayer, P., 2017. Characterizing CO_2 plumes in deep saline formations; comparison and joint evaluation of time-lapse pressure and seismic tomography, *Geophysics,* **82**(4), 1–18.

Hu, R., 2011. Hydraulic tomography: a new approach coupling hydraulic travel time, attenuation and steady shape inversions for high-spatial resolution aquifer characterization, *PhD thesis*, Georg-August-Universität Göttingen.

Hu, R., Brauchler, R., Herold, M. & Bayer, P., 2011. Hydraulic tomography analog outcrop study: combining travel time and steady shape inversion, *J. Hydrol.,* **409,** 350–362.

Illman, W.A., Liu, X., Takeuchi, S., Jim Yeh, T.-C., Ando, K. & Saegusa, H., 2009. Hydraulic tomography in fractured granite: Mizunami underground research site, Japan, *Water Resour. Res.,* **45**(1), W01406.

JafarGandomi, A. & Binley, A., 2013. A bayesian trans-dimensional approach for the fusion of multiple geophysical datasets, *J. appl. Geophys.,* **96,** 38–54.

Klepikova, M., Brixel, B. & Jalali, M., 2020. Transient hydraulic tomography approach to characterize main flowpaths and their connectivity in fractured media, *Adv. Water Resour.,* **136,** 103500.

Klepikova, M., Le Borgne, T., Bour, O., Gallagher, K., Hochreutener, R. & Lavenant, N., 2014. Passive temperature tomography experiments to characterize transmissivity and connectivity of preferential flow paths in fractured media, *J. Hydrol.,* **512,** 549–562.

Lajaunie, M., Maurya, P.K. & Fiandaca, G., 2016. Comparison of Cole–Cole and constant phase angle modeling in time-domain induced polarization, in *Proceedings of the 4th International Workshop on Induced Polarization*.

Liu, Q., Hu, R., Hu, L., Xing, Y., Qiu, P., Yang, H., Fischer, S. & Ptak, T., 2022. Investigation of hydraulic properties in fractured aquifers using cross-well travel-time based thermal tracer tomography: numerical and field experiments, *J. Hydrol.,* **609,** 127751.

Loke, M.H., Acworth, I. & Dahlin, T., 2003. A comparison of smooth and blocky inversion methods in 2D electrical imaging surveys, *Explor. Geophys.,* **34,** 182–187.

Luo, N., Zhao, Z., Illman, W.A., Zha, Y., Mok, C. M.W. & Yeh, T.-C.J., 2023. Three-dimensional steady-state hydraulic tomography analysis with

integration of cross-hole flowmeter data at a highly heterogeneous site, *Water Resour. Res.,* **59**(6), e2022WR034034.

Madsen, L.M., Fiandaca, G. & Auken, E., 2020. 3-D time-domain spectral inversion of resistivity and full-decay induced polarization data - full solution of Poisson's equation and modelling of the current waveform, *Geophys. J. Int.,* **223,** 2101–2116.

Madsen, L.M., Fiandaca, G., Auken, E. & Christiansen, A.V., 2017. Time-domain induced polarization – an analysis of Cole–Cole parameter resolution and correlation using Markov Chain Monte Carlo inversion, *Geophys. J. Int.,* **211,** 1341–1353.

Marshall, D.J. & Madden, T.R., 1959. Induced polarization, a study of its causes, *Geophysics,* **4,** 790–816.

Martin, T. *et al.* , 2021. Inversion of hydraulic conductivity from induced polarisation. Part b: field examples from five countries, in *Proceedings of the NSG2021 1st Conference on Hydrogeophysics*.

Martin, T., Günther, T., Orozco, A.F. & Dahlin, T., 2020. Evaluation of spectral induced polarization field measurements in time and frequency domain, *J. appl. Geophys.,* **180,** 104141.

Maurya, P.K. *et al.*, 2018a. Subsurface imaging of water electrical conductivity, hydraulic permeability and lithology at contaminated sites by induced polarization, *Geophys. J. Int.,* **213,** 770–785.

Maurya, P.K., Fiandaca, G., Christiansen, A.V. & Auken, E., 2018b. Field-scale comparison of frequency- and time-domain spectral induced polarization, *Geophys. J. Int.,* **214,** 1441–1466.

Mollaret, C., Wagner, F., Hilbich, C., Scapozza, C. & Hauck, C., 2020. Petrophysical joint inversion applied to alpine permafrost field sites to image subsurface ice, water, air, and rock contents., *Front. Earth Sci.,* **8,** 85.

Nordsiek, S. & Weller, A., 2008. A new approach to fitting induced-polarization spectra, *Geophysics,* **73**(6), 235–245.

Olhoeft, G.R., 1985. Low-frequency electrical properties, *Geophysics,* **50**(12), 2492–2503.

Olsson, P.I., Fiandaca, G., Larsen, J.J., Dahlin, T. & Auken, E., 2016. Doubling the spectrum of time-domain induced polarization by harmonic de-noising, drift correction, spike removal, tapered gating and data uncertainty estimation, *Geophys. J. Int.,* **207,** 774–784.

Pelton, W., Ward, S., Hallof, P., Sill, W. & Nelson, P., 1978. Mineral discrimination and removal of inductive coupling with multifrequency IP, *Geophysics,* **43,** 588–609.

Refsgaard, J.C., Christensen, S., Sonnenborg, T.O., Seifert, D., Hojberg, A.L. & Troldborg, L., 2012. Review of strategies for handling geological uncertainty in groundwater flow and transport modeling, *Adv. Water Resour.,* **36,** 36–50.

Ren, S., Zhang, Y., Jim Yeh, T.-C., Wang, Y. & Carr, B.J., 2021. Multiscale hydraulic conductivity characterization in a fractured granitic aquifer: The evaluation of scale effect, *Water Resour. Res.,* **57**(9), e2020WR028482.

Revil, A. & Florsch, N., 2010. Determination of permeability from spectral induced polarization in granular media, *Geophys. J. Int.,* **181,** 1480–1498.

Revil, A., Binley, A., Mejus, L. & Kessouri, P., 2015. Predicting permeability from the characteristic relaxation time and intrinsic formation factor of complex conductivity spectra, *Water Resour. Res.,* **51,** 6672–6700.

Revil, A., Koch, K. & Holliger, K., 2012. Is it the grain size or the characteristic pore size that controls the induced polarization relaxation time of clean sands and sandstones?, *Water Resour. Res.,* **48,** W05602.

Ringel, L.M., Jalali, M. & Bayer, P., 2022. Characterization of the highly fractured zone at the Grimsel test site based on hydraulic tomography, *Hydrol. Earth Syst. Sci.,* **26,** 6443–6455.

Robinson, J., Slater, L., Weller, A., Keating, K., Robinson, T., Rose, C. & Parker, B., 2018. On permeability prediction from complex conductivity measurements using polarization magnitude and relaxation time, *Water Resour. Res.,* **54,** 3436–3452.

Römhild, L.,, Hu, L., Meyer, L. & Bayer, P., 2022a. Imaging hydraulic conductivity in near-surface aquifers by complementing cross-borehole induced polarization with hydraulic experiments, *Adv. Water Resour.,* **170,** 104322.

Römhild, L., Sonntag, M., Kiyan, D., Rogers, R., Rath, V. & Börner, J.H., 2022b. Anisotropic broadband spectral induced polarization (SIP) data of black shale and mudstone from the Moffat Shale Group (Ireland), V. 1.0. GFZ Data Services. https://doi.org/10.5880/fidgeo.2022.034.

Römhild, L., Ringel, L.M., Liu, Q., Hu, L., Ptak, T. & Bayer, P., 2024. Hybrid discrete fracture network inversion of hydraulic tomography data from a fractured-porous field site, *Water Resour. Res.,* **60,** e2023WR036035.

Rücker, C., Günther, T. & Wagner, F.M., 2017. pygimli: an open-source library for modelling and inversion in geophysics, *Comput. Geosci.,* **109,** 106–123.

Schön, J., 2015. *Physical Properties of Rocks - Fundamentals and Principles of Petrophysics,* 2nd edn, Vol. **65,** Elsevier.

Schwarz, G., 1962. A theory of the low-frequency dielectric dispersion of colloidal particles in electrolyte solution, *J. Phys. Chem.,* **66,** 2636–2642.

Seigel, H.O., 1959. Mathematical formulation and type curves for induced polarization, *Geophysics,* **24,** 547–565.

Singha, K., Day-Lewis, F.D., Johnson, T. & Slater, L.D., 2015. Advances in interpretation of subsurface processes with time-lapse electrical imaging, *Hydrol. Proc.,* **29**(6), 1549–1576.

Slater, L. & Lesmes, D.P., 2002. Electrical-hydraulic relationships observed for unconsolidated sediments, *Water Resour. Res.,* **38**(10), 1213.

Slater, L., 2007. Near surface electrical characterization of hydraulic conductivity: from petrophysical properties to aquifer geometries - a review, *Surv. Geophys.,* **28,** 169–197.

Somogyvari, M. & Bayer, P., 2017. Field validation of thermal tracer tomography for reconstruction of aquifer heterogenity, *Water Resour. Res.,* **53**(6), 5070–5084.

Somogyvári, M., Kühn, M. & Reich, S., 2019. Reservoir-scale transdimensional fracture network inversion, *Advances in Geosciences,* **49,** 207–214.

Tarasov, A. & Titov, K., 2013. On the use of the Cole–Cole equations in spectral induced polarization, *Geophys. J. Int.,* **195,** 352–356.

Thalund-Hansen, R., Troldborg, M., Levy, L., Christiansen, A.V., Bording, T.S. & Bjerg, P.L., 2023. Assessing contaminant mass discharge uncertainty with application of hydraulic conductivities derived from geoelectrical cross-borehole induced polarization and other methods, *Water Resour. Res.,* **59,** WR034360.

Thibaut, R., Laloy, E. & Hermans, T., 2021. A new framework for experimental design using Bayesian evidential learning: the case of wellhead protection area, *J. Hydrol.,* **603**(A), 126903.

Titov, K., Tarasov, A., Ilyin, Y., Seleznev, N. & Boyd, A., 2010. Relationships between induced polarization relaxation time and hydraulic properties of sandstone, *Geophys. J. Int.,* **180,** 1095–1106.

Turco, F., Azevedo, L., Grana, D., Crutchley, G. & Gorman, A., 2021. Characterization of gas hydrate systems on the Hikurangi margin (New Zealand) through geostatistical seismic and petrophysical inversion, *Geophysics,* **86**(6), R825–R838.

van der Walt, S., Schönberger, J., Nunez-Iglesias, J., Boulogne, F., Warner, J., Yager, N., Gouillart, E. & Yu, T., 2014. scikit-image: image processing in python, *PeerJ,* **2,** e453.

Vinegar, H.J. & Waxman, M.H., 1984. Induced polarization of shaly sands, *Geophysics,* **49**(8), 1267–1287.

Wang, Z., Bovik, A., Sheik, H. & Simoncelli, E., 2004. Image quality assessment: From error visibility to structural similarity, *IEEE Trans. Image Proc.,* **13**(4), 600–612.

Weigand, M. & Kemna, A., 2016. Relationship between cole–cole model parameters and spectral decomposition parameters derived from sip data, *Geophys. J. Int.,* **205,** 1414–1419.

Weller, A., Seichter, M. & Kampke, A., 1996. Induced-polarization modelling using complex electrical conductivities, *Geophys. J. Int.,* **127,** 387–398.

Weller, A., Slater, L. & Nordsiek, S., 2013. On the relationship between induced polarization and surface conductivity: Implications for petrophysical interpretation of electrical measurements, *Geophysics,* **78**(5), D315–D325.

Weller, A., Slater, L., Binley, A., Nordsiek, S. & Xu, S., 2015. Permeability prediction based on induced polarization: Insights from measurements on sandstone and unconsolidated samples spanning a wide permeability range, *Geophysics,* **80**(2), D161–D173.

Weller, A., Zhang, Z., Slater, L., Kruschwitz, S. & Halisch, M., 2016. Induced polarization and pore radius - a discussion, *Geophysics,* **81**(5), D519–D526.

Yang, H., Hu, R., Qiu, P., Liu, Q., Xing, Y., Tao, R. & Ptak, T., 2020. Application of wavelet de-noising for travel-time based hydraulic tomography, *Water,* **12**(6), 1533.

Yeh, J. & Liu, S., 2000. Hydraulic tomography: development of a new aquifer test method, *Water Resour. Res.,* **36**(8), 2095–2105.

You, X., Liu, S., Dai, C., Guo, Y., Zhong, G. & Duan, Y., 2020. Contaminant occurrence and migration between high- and low-permeability zones in groundwater systems: a review, *Sci. Total Environ.,* **743,** doi:10.1016/j.scitotenv.2020.140703.

Zelt, C.A. & Smith, R.B., 1992. Seismic traveltime inversion for 2-d crustal velocity structure, *Geophys. J. Int.,* **108,** 16–34.

Zha, Y., Yeh, T.-C.J., Illman, W.A., Tanaka, T., Bruines, P., Onoe, H. & Saegusa, H., 2015. What does hydraulic tomography tell us about fractured geological media? a field study and synthetic experiments, *J. Hydrol.,* **531,** 17–30.

Zhao, Z., Illman, W.A., Yeh, T.-C.J., Berg, S.J. & Mao, D., 2015. Validation of hydraulic tomography in an unconfined aquifer: a controlled sandbox study, *Water Resour. Res.,* **51,** 4137–4155.

Zhao, Z., Illman, W.A., Zha, Y., Yeh, J., Mok, C. M.B., Berg, S.J. & Han, D., 2019. Transient hydraulic tomography analysis of fourteen pumping tests at a highly heterogeneous multiple aquifer-aquitard system, *Water,* **11**(9), doi:10.3390/w11091864.

Zhao, Z., Luo, N. & Illman, W.A., 2023. Geostatistical analysis of high-resolution hydraulic conductivity estimates from the hydraulic profiling tool and integration with hydraulic tomography at a highly heterogeneous field site, *J. Hydrol.,* **617,** doi:10.1016/j.jhydrol.2023.129060.

Zisser, N., Kemna, A. & Nover, G., 2010. Relationship between low-frequency electrical properties and hydraulic permeability of low-permeability sandstones, *Geophysics,* **75**(3), E131–E141.